Supporting Information for Publication of Article in Soft Matter

Nematic Growth of Microtubules that Changed into Giant Spiral Structure Through Partial Depolymerization and Subsequent Dynamic Ordering

Kiyotaka Shigehara[1], Hiroki Kudoh[1], Saori Mori[1], Yoshiki Tamura[2], Akira Kakugo[2,3], Ryuzo Kawamura[2,†], Hidemitsu Furukawa[4], Jian Ping Gong[2], Hiroyasu Masunaga[5], Tomomi Masui[6], Satoshi Koizumi[6] and Kazuhiro Shikinaka[1,*]

[1]Graduate School of Engineering, Tokyo University of Agriculture and Technology, Koganei, Tokyo 184-8588, Japan

[2]Faculty of Advanced Life Science, Hokkaido University, Sapporo, Hokkaido 060-0810, Japan

[3]PRESTO, Japan Science and Technology Agency, Sapporo, Hokkaido 060-0810, Japan

[4]Department of Mechanical Systems Engineering, Graduate School of Science and Engineering, Yamagata University, Yonezawa, Yamagata 992-8510, Japan

[5]Experimental Research Division, SPring-8, Japan Synchrotron Radiation Research Institute, Sayo-ku, Hyogo 679-5198, Japan

[6]Advanced Science Research Center, Japan Atomic Energy Agency, Naka, Ibaraki 319-1195, Japan

†Present address: Cell Mechanics Research Group BioMedical Research Institute,

National Institute of Advanced Industrial Science and Technology, Tsukuba, Ibaraki

305-8562, Japan.

RECEIVED DATE (to be automatically inserted after your manuscript is accepted if required according to the journal that you are submitting your paper to)

*Author to whom correspondence should be addressed: E-mail: k-shiki@cc.tuat.ac.jp (K.S.) TEL/FAX: +81-42-388-7406

RUNNING HEAD: Nematic Growth of Microtubules that Changed into Giant Spiral Structure

Descriptions of the Movies

Movie 1

A time-lapse movie showing the two-dimensional scattering patterns from MTs in their ordered alignments at 2 mm from the warm terminal during incubation period from 1 to 30 min. The images of the scattering patterns were obtained at a frame size of 3000 × 3000 pixels and a pixel size of 150 × 150 μm^2 using the RIGAKU RAXIS IV++ imaging plate detector system (see the Observation subsection in the Materials and Methods section of the manuscript) and were recorded at intervals of 20 s with an exposure time of 40 s. The play time is accelerated by a factor of 120 (*i.e.,* 15 s movie = 30 min experimental time). The partly still images are shown in Figure 2 (a).

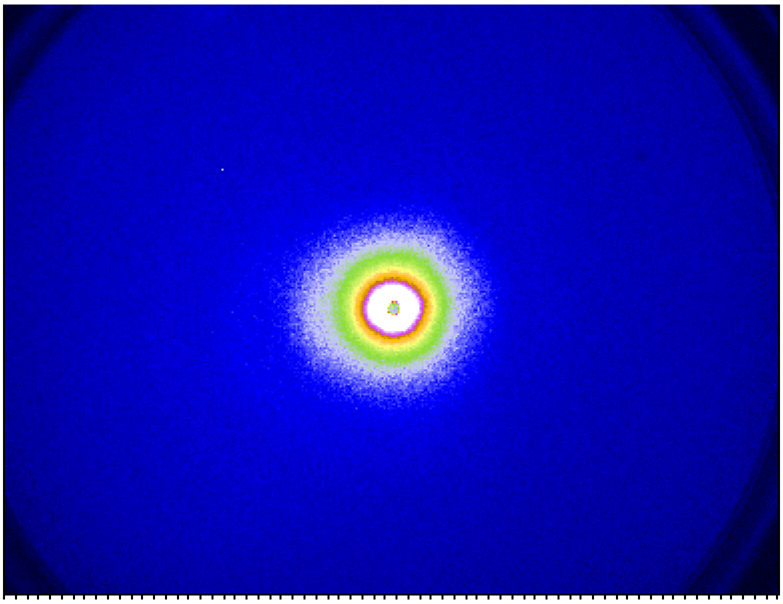

Movie 2

A time-lapse movie showing the two-dimensional scattering patterns from MTs in their ordered alignments at 8 mm position from the warm terminal during incubation period from 1 to 30 min. The images of the scattering patterns were obtained at a frame size of 3000 × 3000 pixels and a pixel size of 150 × 150 μm^2 using the RIGAKU RAXIS IV++ imaging plate detector system (see the Observation subsection in the Materials and Methods section of the manuscript) and were recorded at intervals of 20 s with an exposure time of 40 s. The play time is accelerated by a factor of 120 (*i.e.,* 15 s movie = 30 min experimental time). The partly still images are shown in Figure 2 (b).

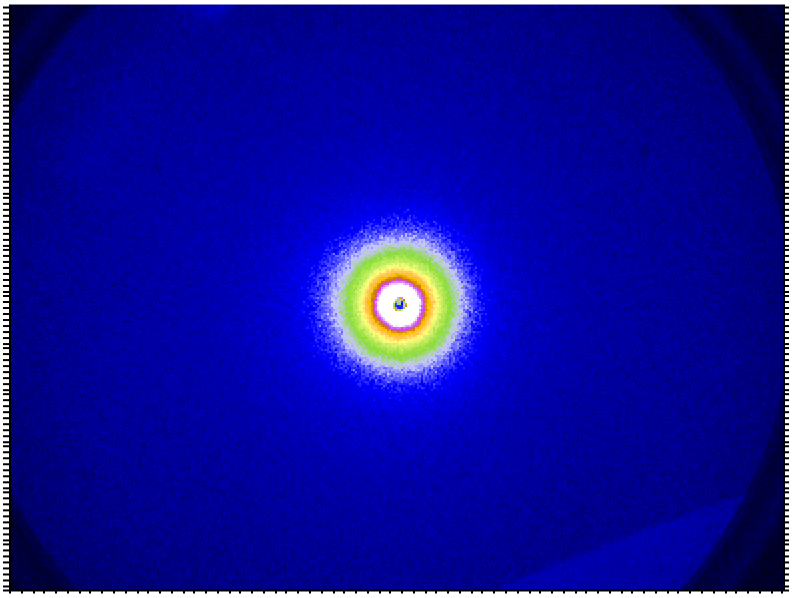

Movie 3

Movies of two-dimensional scattering images from MTs in their ordered alignments at 2 to 15 mm positions from the warm terminal with an interval of 0.5 or 1 mm at 50 min of incubation period. The images of the scattering patterns were obtained at a frame size of 3000 × 3000 pixels and a pixel size of 150 × 150 μm^2 using the RIGAKU RAXIS IV++ imaging plate detector system (see the Observation subsection in the Materials and Methods section of the manuscript) and were recorded at intervals of 40 s with an exposure time of 20 s.

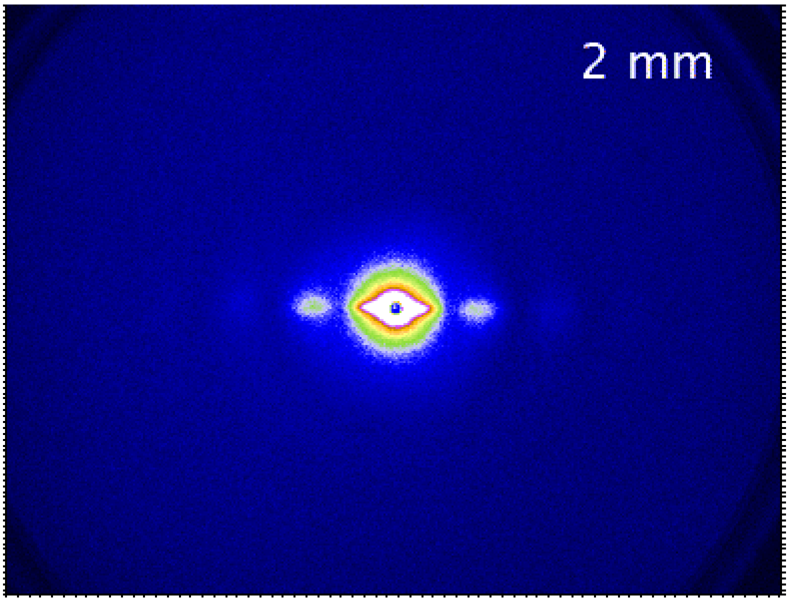

Estimation adequacy of analysis of MT length from scattering curves

For the model calculation of scattering curves, MTs were regarded as hollow cylinders. The scattering profiles were simulated according to the following equations;

$$P(q) = \phi \cdot \pi (R_{\mathrm{shell}}^2 - R_{\mathrm{core}}^2) L \cdot (\Delta\rho)^2 \int_0^1 \Psi^2 [q, R_{\mathrm{shell}}(1-x^2)^{1/2}, R_{\mathrm{core}}(1-x^2)^{1/2}] \left(\frac{\sin(qHx)}{qHx} \right)^2 dx$$

……………....(1)

$$\Psi(q,y,z) = \frac{2}{1-(R_{\mathrm{core}}/R_{\mathrm{shell}})^2} \left[\frac{J_1(qR_{\mathrm{shell}}(1-x^2)^{1/2})}{qR_{\mathrm{shell}}(1-x^2)^{1/2}} - \left(\frac{R_{\mathrm{core}}}{R_{\mathrm{shell}}} \right)^2 \frac{J_1(qR_{\mathrm{core}}(1-x^2)^{1/2})}{qR_{\mathrm{core}}(1-x^2)^{1/2}}] \right]$$

……………....(2)

$$J_1(x) \equiv \left(\frac{x}{2} \right) \sum_{l=0}^{\infty} \frac{(-1)^l}{l!(l+1)!} \left(\frac{x}{2} \right)^{2l}$$

……………....(3)

$$H = L/2$$

……………....(4)

where *P(q)*, *q*, and ***L*** are the shape factor, the scattering vector, and the cylinder (MT) length, respectively. R_{shell} and R_{core} are the shell and core radii of a cylinder. ρ and ψ are the scattering length density and volume fraction of a cylinder. x is the order parameter.

The theoretical curves of a hollow cylinder at various lengths were shown in Figure S1. From this figure (especially q = 0.19 Å in right part), it is clear that the valleys of curves between peaks become shallower with the decrease in the cylinder length.

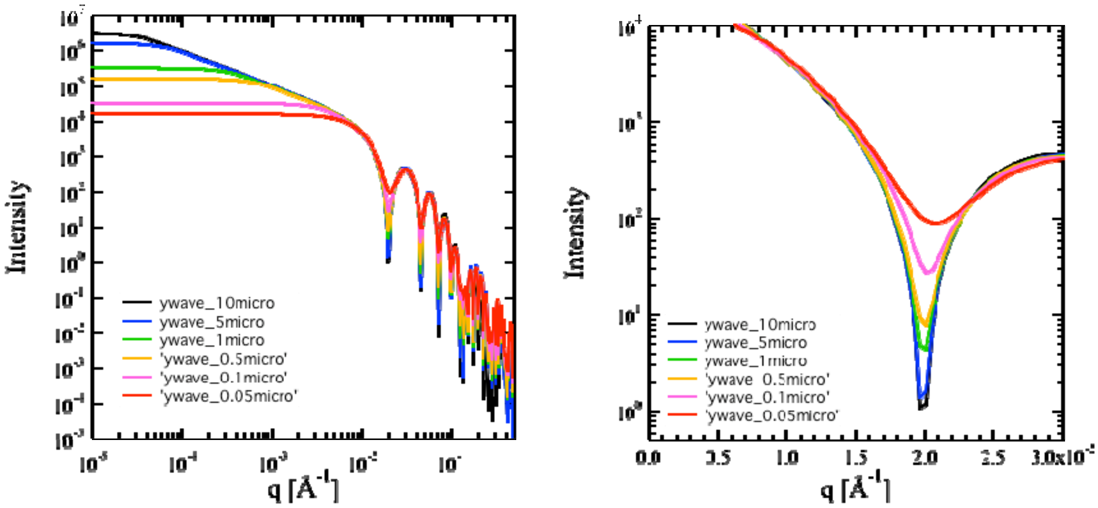

Figure S1 Model calculations showing how ***L*** affects the relative scattering intensity : ***L*** = 10 μm (black), 5 μm (blue), 1 μm (green), 0.5 μm (yellow), 0.1 μm (pink), 0.05 μm (red). In these calculations, R_{shell} and R_{core} is 14.35 nm and 9.65 nm, respectively.

Next, we estimated the contribution of term which depends on R_{shell} and R_{core} (framed by blue square) or on ***L*** (framed by red square), as shown in eq.(5).

$$P(q) = \phi \cdot \pi (R_{\mathrm{shell}}^2 - R_{\mathrm{core}}^2) L \cdot (\Delta\rho)^2 \int_0 \boxed{\Psi^2[q, R_{\mathrm{shell}}(1-x^2)^{1/2}, R_{\mathrm{core}}(1-x^2)^{1/2}]} \boxed{\left(\frac{\sin(qHx)}{qHx}\right)^2} dx \qquad \text{.................(5)}$$

The term which depends on R_{shell} and R_{core} (ψ^2) changes with the order parameter, x ($0 \leq x \leq 1$). The dependence of ψ^2 on x was shown in Figure S2. At q = 0.19 Å, ψ^2 is the finite value except for $0 \leq x \leq 0.2$, *i.e.*, this term is not attributed to the generation of valleys of theoretical curves in Figure S1.

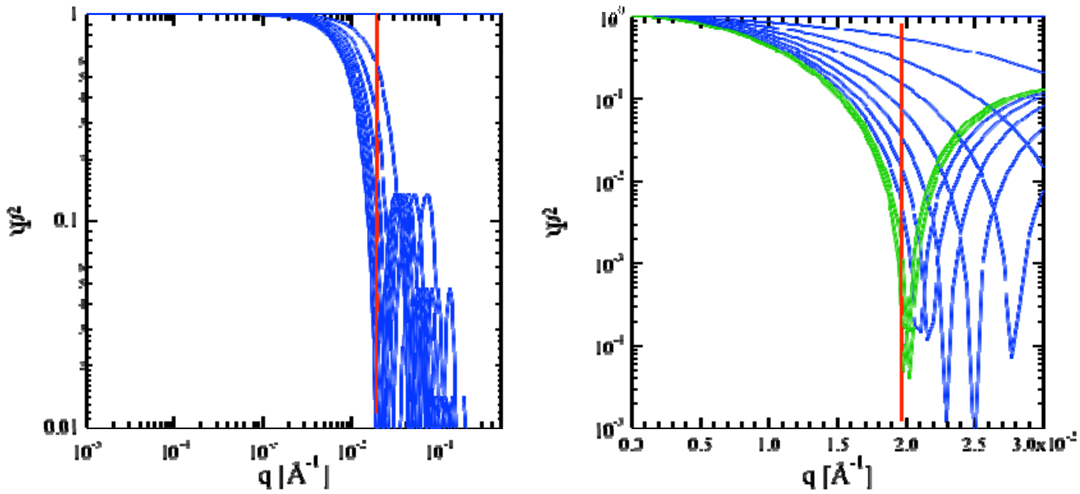

Figure S2 The dependence of ψ^2 on x. The red line in the graph indicates the q value equal to the position of a valley in the theoretical curve of Figure S1 (q = 0.19 Å).

The term which depends on $\boldsymbol{L}$ ($(\sin(qHx)/qHx)^2$) also changes with x ($0 \leq x \leq 1$). Here, $(\sin(qHx)/qHx)^2$ was calculated at various $\boldsymbol{L}$ and x. As shown in Figure S3, the valley was obviously distinguished at q = 0.19 Å, for instance, that is; this term is attributed to the generation of valleys of theoretical curves in Figure S1. By contrast, $(\sin(qHx)/qHx)^2$ is the finite value at $\boldsymbol{L}$ = 0.1 μm, and x = 0.1 or 0.5 (Figure S3 (a)). This is the reason for the valleys being shallower in the theoretical curves.

Thus, the valleys in theoretical curves become shallow with a decrease in the $\boldsymbol{L}$ value of a cylinder, and therefore the $\boldsymbol{L}$ value of MT can be estimated by the curve fitting method.

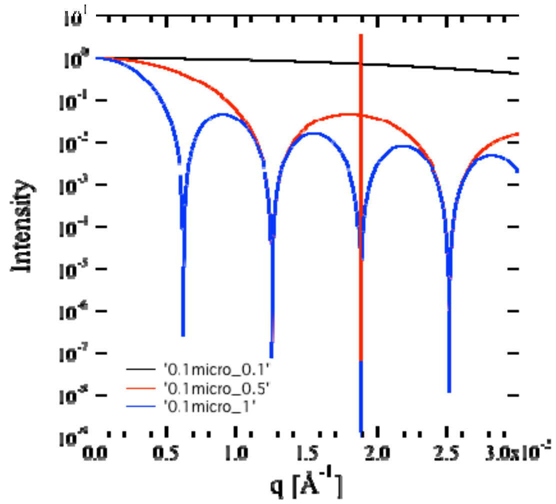

Figure S3 (a) The dependence of $(\sin(qHx)/qHx)^2$ on x at $\boldsymbol{L}$ = 0.1 μm (x = 0.1 (black), 0.5 (red), 1 (blue)). The red line in the graph indicates the q value equal to the position of a valley in the theoretical curve of Figure S1 (q = 0.19 Å).

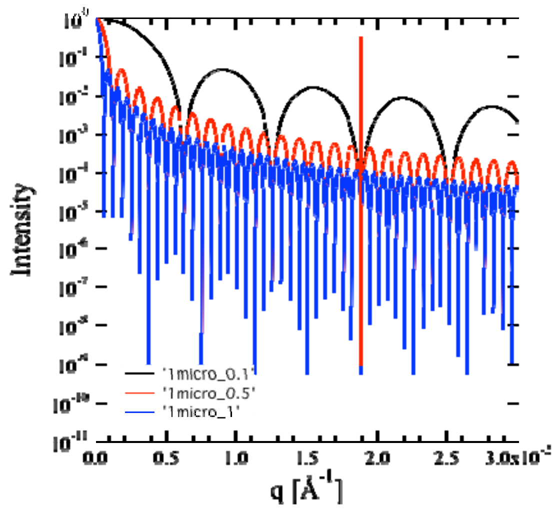

Figure S3 (b) The dependence of $(\sin(qHx)/qHx)^2$ on x at $\boldsymbol{L}$ = 1 μm (x = 0.1 (black), 0.5 (red), 1 (blue)). The red line in the graph indicates the q value equal to the position of a valley in the theoretical curve of Figure S1 (q = 0.19 Å).

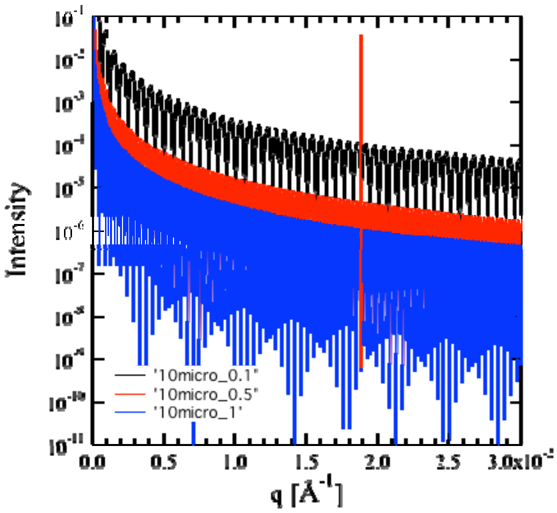

Figure S3 (c) The dependence of $(\sin(qHx)/qHx)^2$ on x at $\boldsymbol{L}$ = 10 μm (x = 0.1 (black), 0.5 (red), 1 (blue)). The red line in the graph indicates the q value equal to the position of a valley in the theoretical curve of Figure S1 (q = 0.19 Å).

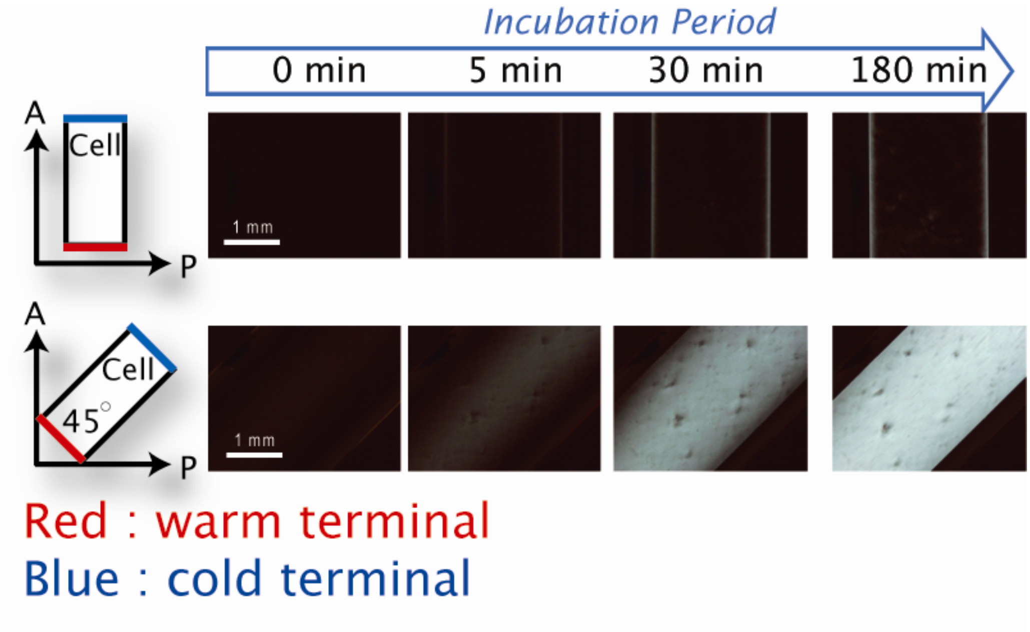

Figure S4 Time-lapse POM images of the ordered alignment of MTs in the rectangular thin glass cell ***without temperature gradient*** at near the 8 mm position from the warm terminal, where the arrows of A and P represent the analyzer and polarizer setting direction. The angle between the cell and the analyzer was illustrated leftmost. The warm terminal of each cell was the bottom side.

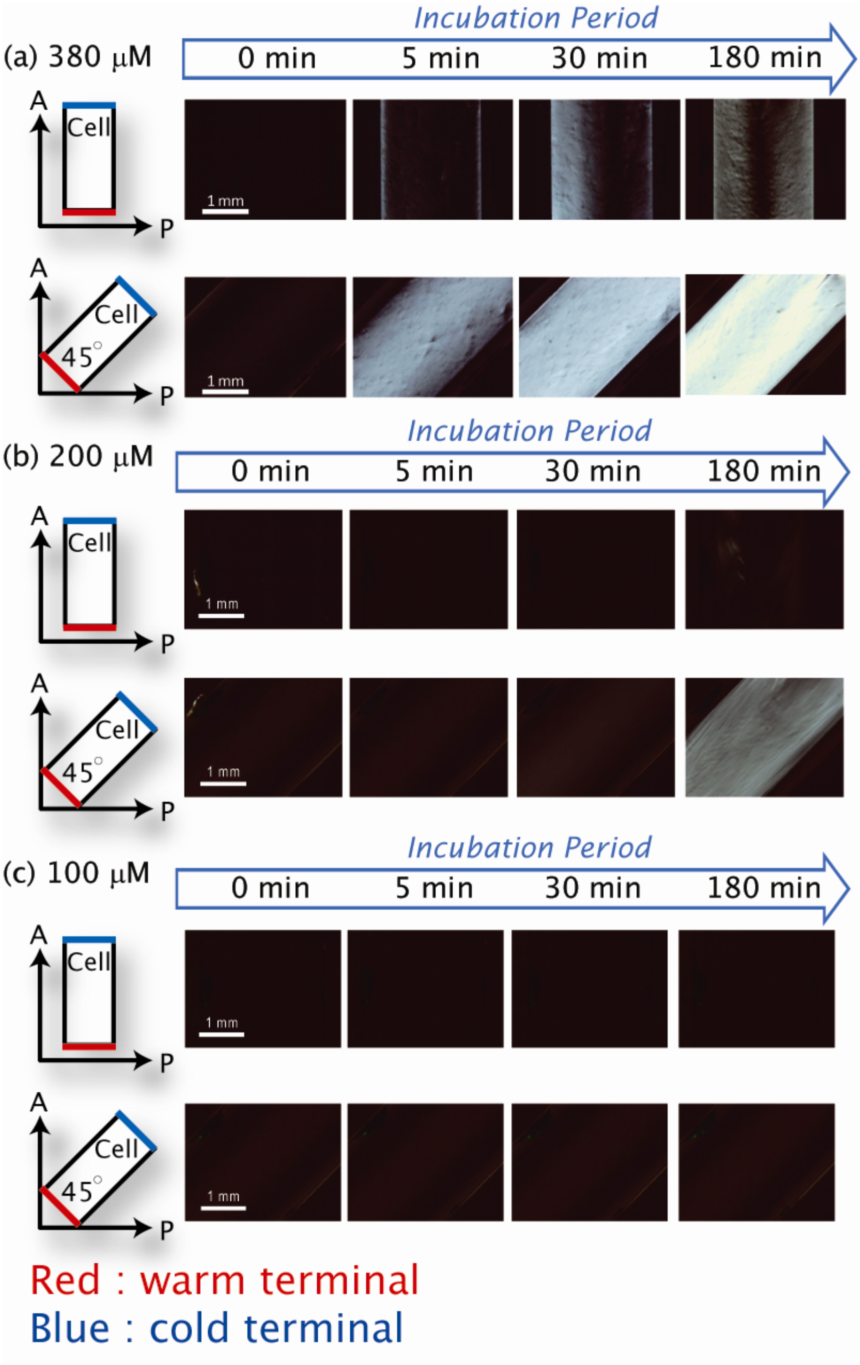

Figure S5 Time-lapse POM images of the ordered alignment of MTs in the rectangular thin glass cell under temperature gradient ***at various concentrations of tubulin*** ((a) equals to the result shown in Figure 8) at near the 8 mm position from the warm terminal, where the arrows of A and P represent the analyzer and polarizer setting direction. The angle between the cell and the analyzer was illustrated leftmost. The warm terminal of each cell was the bottom side.

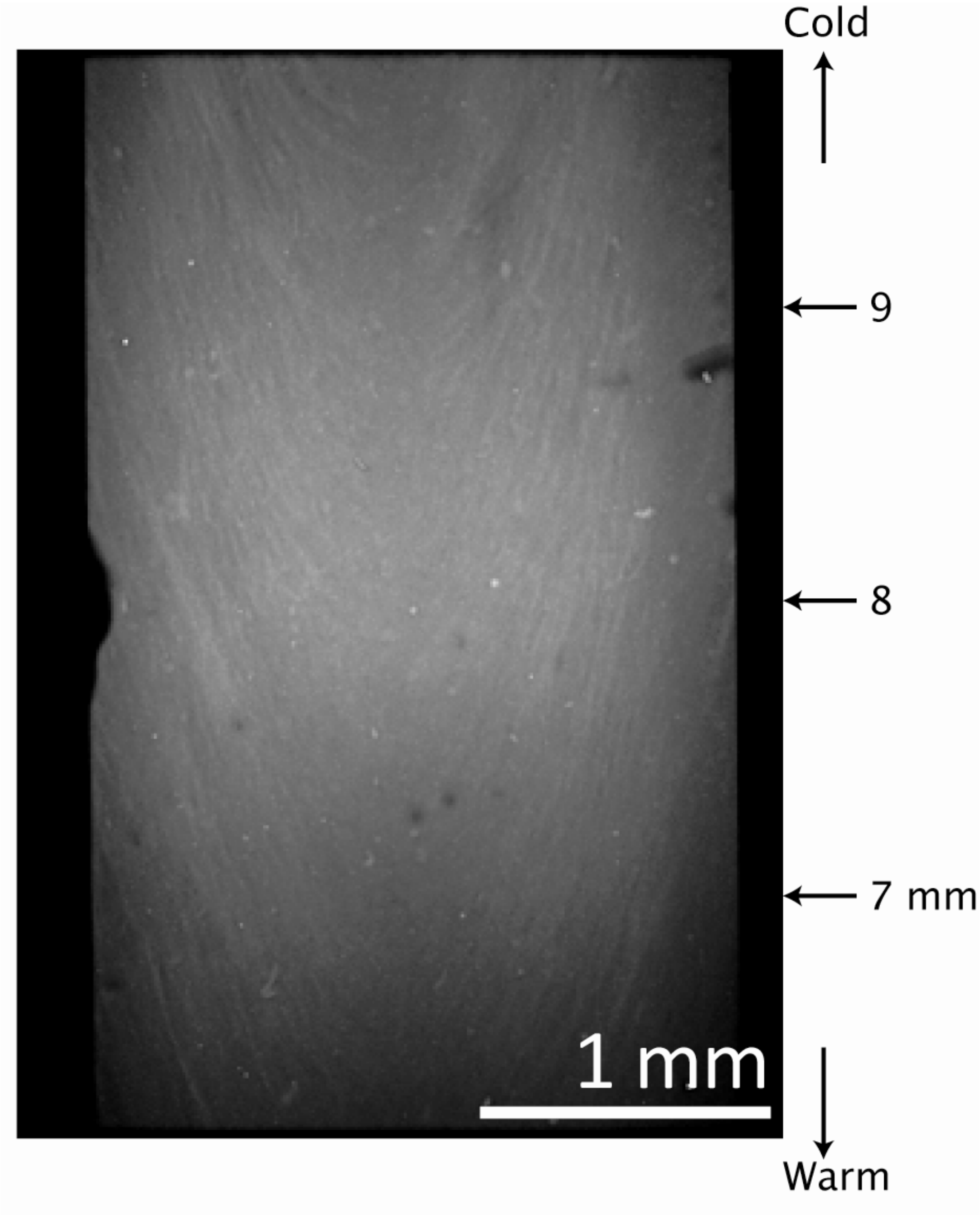

Figure S6 FM image of the ordered alignments of MTs at near the 8 mm position from the warm terminal at 60 min of the incubation period. (This image is same to Figure 7 (a))